INTERNATIONAL JOURNAL FOR NUMERICAL METHODS IN FLUIDS
Int. J. Numer. Meth. Fluids 2008; **58**:591–624
DOI: 10.1002/fld.1758

Semi-coupled air/water immersed boundary approach for curvilinear dynamic overset grids with application to ship hydrodynamics

Juntao Huang, Pablo M. Carrica and Frederick Stern*,†

IIHR-Hydroscience and Engineering, The University of Iowa, Iowa City, IA 52242, U.S.A.

SUMMARY

For many problems in ship hydrodynamics, the effects of air flow on the water flow are negligible (the frequently called free surface conditions), but the air flow around the ship is still of interest. A method is presented where the water flow is decoupled from the air solution, but the air flow uses the unsteady water flow as a boundary condition. The authors call this a semi-coupled air/water flow approach. The method can be divided into two steps. At each time step the free surface water flow is computed first with a single-phase method assuming constant pressure and zero stress on the interface. The second step is to compute the air flow assuming the free surface as a moving immersed boundary (IB). The IB method developed for Cartesian grids (*Annu. Rev. Fluid Mech.* 2005; **37**:239–261) is extended to curvilinear grids, where no-slip and continuity conditions are used to enforce velocity and pressure boundary conditions for the air flow. The forcing points close to the IB can be computed and corrected under a sharp interface condition, which makes the computation very stable. The overset implementation is similar to that of the single-phase solver (*Comput. Fluids* 2007; **36**:1415–1433), with the difference that points in water are set as IB points even if they are fringe points. Pressure–velocity coupling through pressure implicit with splitting of operators or projection methods is used for water computations, and a projection method is used for the air. The method on each fluid is a single-phase method, thus avoiding ill-conditioned numerical systems caused by large differences of fluid properties between air and water. The computation is only slightly slower than the single-phase version, with complete absence of spurious velocity oscillations near the free surface, frequently present in fully coupled approaches. Validations are performed for laminar Couette flow over a wavy boundary by comparing with the analytical solution, and for the surface combatant model David Taylor Model Basin (DTMB) 5512 by comparing with Experimental Fluid Dynamics (EFD) and the results of two-phase level set computations. Complex flow computations are demonstrated for the ONR Tumblehome DTMB 5613 with superstructure subject to waves and wind, including 6DOF motions and broaching in SS7 irregular waves and wind. Copyright © 2008 John Wiley & Sons, Ltd.

Received 5 July 2007; Revised 18 December 2007; Accepted 19 December 2007

---

*Correspondence to: Frederick Stern, IIHR-Hydroscience and Engineering, The University of Iowa, Iowa City, IA 52242, U.S.A.

†E-mail: frederick-stern@uiowa.edu

Contract/grant sponsor: ONR; contract/grant numbers: N00014-01-1-0073, N00014-06-1-0420

KEY WORDS: free surface flows; level set method; semi-coupled method; immersed boundary; curvilinear and dynamic overset grids; ship hydrodynamics

1. INTRODUCTION

There is an increasing interest on air/water turbulent flows around ships and environmental effects on ship hydrodynamics. Winds and waves and their effects on forces and ship motions, air wakes studies, and thermal transport of high-temperature exhaust gases for moving ships with complicated superstructures are some of the problems of interest in which both the air and water phases need to be computed. However, the coupled computation of the air and water flows across a free surface in complex geometries is a significant numerical challenge. Large differences of fluid properties between air and water cause extremely ill-conditioned numerical systems. Nevertheless, for a significantly large class of problems the air flow has little effect on the water solution, affecting mostly the small scale such as spray production and small-wavelength wave generation. Large-amplitude, long-wavelength waves are generated by wind on reaches of several hundred miles, and thus the effect of air on the computational water region in the near field of a ship, typically a few ship lengths in size, can be neglected. Shorter waves can be generated much closer to the ship, but their effect on the ship flow is most often negligible.

For large-scale problems, classical computational fluid dynamics (CFD) for ship hydrodynamics free surface flows typically decouple the water from the air by imposing kinematic and approximate dynamic free surface boundary conditions, thus solving the water side only. Surface tracking [1] and surface capturing [2–4] methods have been proposed that solve the water flow ignoring air effects. Similarly, air flows around the superstructure of a surface ship are most frequently computed by ignoring the water flow, assuming a flat boundary at the air/water interface [5, 6].

Fully coupled two-phase approaches typically use the level set method, originally introduced by Osher and Sethian [7], or the volume of fluid method [8, 9], or refinements of these methods. Examples of ship flow computations with two-phase approaches can be found in [10–12]. All these computations have shown promising results but suffer from the large difference in fluid properties between air and water, which causes ill-conditioned numerical systems that may cause instabilities and a certain level of spurious velocities near the interface. In addition, with the exception of Huang *et al.* [12], these two-phase solutions concentrated on the water flow only, with little or no discussion on the air flow.

In Huang *et al.* [12], the authors present the code CFDShip-Iowa version 5, a curvilinear solver for two-phase free surface flows developed following the basic architecture of CFDShip-Iowa version 4, a single-phase solver [3]. The code uses a level set approach to capture the free surface. Although the results were satisfactory for several example applications, including the air/water free surface flow around a model surface combatant, limitations were found when implementing overset grids. Because of the large differences in fluid properties, the two-phase method is very sensitive to small discontinuities between two different overlapping grids. These discontinuities are specially amplified in the pressure equation when the pressure gradients are divided by the density that has a ratio of 1:830. These issues are particularly important if complex geometries and motions are to be simulated in a structured curvilinear grid approach.

For large-scale problems, a semi-coupled air/water level set method is developed here (CFDSHIP-Iowa version 4.5), which makes approximations consistent with the classical kinematic and approximate dynamic free surface boundary conditions, and is significantly faster and robust

DOI: 10.1002/fld

than most coupled two-phase level set approaches for its single-phase nature. The method is semi-coupled, in the sense that the water flow uses kinematic and dynamic free surface boundary conditions ignoring the flow in air, while the air flow uses the free surface and velocity information from the water utilizing an immerse boundary method. The method allows easy implementation of dynamic overset grids, an attractive quality for the simulation of complex motions. The price to pay is the inability to treat air entrainment or wind-induced waves. For most ship applications, the proposed approach is an acceptable approximation, including analysis of environmental conditions and air wakes around a ship in motion with complex superstructures, maneuverability and seakeeping under strong winds, capsizing, etc.

The term ‘immersed boundary method’ (IB method) was first used in reference to a method developed by Peskin [13] to simulate cardiac mechanics and associated blood flow. The distinguishing feature of this method was that the entire simulation was carried out on a Cartesian grid, which did not conform to the physical geometry [14]. Over the past decades, numerous modifications and refinements have been proposed and a number of variants of this approach now exist, and the improved method can simulate the flow with moving boundaries. In this paper, an IB method is used to impose the boundary conditions for air on the water interface in curvilinear grids. Since in level set methods the interface is not coincident with the grid points, an IB method is convenient because it can treat a moving free surface regardless of how complicated the topological changes are. The computation is very stable because the forcing points close to the IB can be computed and corrected under a sharp interface condition, particularly by computing the pressure on all points neighboring the boundary.

Validations are performed for laminar Couette flow over a wavy boundary by comparing with the analytical solution, the surface combatant David Taylor Model Basin (DTMB) 5512 against EFD data and the results of two-phase level set computations. Steady-state computations of the air/water flow around the ONR Tumblehome model DTMB 5613 with superstructure and bilge keels are demonstrated. Finally, the problem of broaching of an autopilot-controlled ONR Tumblehome in irregular short-crested waves in SS7 with and without wind is analyzed.

2. MATHEMATICAL MODEL

2.1. Governing equations

It is assumed that the air/water two-phase moving interface problem is a free surface problem, where the presence of air does not affect the water flow, but the effect of the water flow and the free surface are important to compute the air flow. The air/water interface is regarded as a no-slip moving boundary for the air flow.

The Reynolds-Averaged Navier–Stokes (RANS) momentum and mass conservation equations for either water or air are expressed as

$$\frac{\partial u_i}{\partial t}+u_j\frac{\partial u_i}{\partial x_j}=-\frac{\partial \hat{p}}{\partial x_i}+\frac{\partial}{\partial x_j}\left[Re_{\text{eff}}^{-1}\left(\frac{\partial u_i}{\partial x_j}+\frac{\partial u_j}{\partial x_i}\right)\right]+S_i \tag{1}$$

$$\frac{\partial u_j}{\partial x_j}=0 \tag{2}$$

DOI: 10.1002/fld

where the piezometric pressure is

$$\hat{p}=p+\frac{z}{Fr^2}+\frac{2}{3}k, \quad p=\frac{p_{\text{abs}}}{\rho_l U_0^2}$$

S_i is a body force due, for instance, to a propeller model, $Re=\rho_l U_0 L_0/\mu_l$ ($l=w$ for water and $l=a$ for air), $Re_{\text{eff}}^{-1}=1/Re+\gamma_{\text{t}}$, with γ_{t} the non-dimensional turbulent viscosity obtained from a turbulence model, and $Fr=U_0/\sqrt{gL}$. The subscript 'abs' stands for the absolute dimensional value of any property or variable, and U_0 and L are the reference velocity and length, usually the ship's speed and length between fore and aft perpendiculars. All variables and properties are non-dimensionalized with U_0, L, and corresponding fluid properties (water or air).

2.1.1. Coordinate transformation. The governing equations are transformed from the physical domain in Cartesian coordinates (x, y, z, t) into the computational domain in non-orthogonal curvilinear coordinates (ξ, η, ζ, τ) [15], where all cells are cubes with unit sides. A partial transformation is used in which only the independent variables are transformed, leaving the velocity components U_k in the base coordinates [16].

2.1.2. Hydrodynamic equations. The transformed mass conservation equation reads

$$\frac{1}{J}\frac{\partial}{\partial \xi^j}(b_k^j U_k)=0 \tag{3}$$

and the momentum equation

$$\frac{\partial U_i}{\partial \tau}+\frac{1}{J}\frac{\partial}{\partial \xi^j}(\breve{U}^j U_i)=-\frac{1}{J}b_i^j\frac{\partial \hat{p}}{\partial \xi^j}+\frac{1}{J}\frac{\partial}{\partial \xi^j}\left[\frac{1}{J}Re_{\text{eff}}^{-1}b_l^j\left(b_l^k\frac{\partial U_i}{\partial \xi^k}+b_i^k\frac{\partial U_l}{\partial \xi^k}\right)\right]+S_i \tag{4}$$

where $\breve{U}^j=b_l^j U_l$ is the contravariant velocity.

2.1.3. Turbulence model. Menter's blended k–ω/k–ε model of turbulence is adopted [17]. The dimensionless equations for γ_{t}, k and ω can be expressed in curvilinear coordinates

$$\gamma_{\text{t}}=\frac{k}{\omega} \tag{5}$$

$$\frac{\partial k}{\partial \tau}+\frac{1}{J}(b_l^j U_l)\frac{\partial k}{\partial \xi^j}=\frac{1}{J}\frac{\partial}{\partial \xi^j}\left[\frac{1}{J}\left(\frac{1}{Re}+\sigma_k\gamma_{\text{t}}\right)b_l^j b_l^m\frac{\partial k}{\partial \xi^m}\right]+S_k \tag{6}$$

$$\frac{\partial \omega}{\partial \tau}+\frac{1}{J}(b_l^j U_l)\frac{\partial \omega}{\partial \xi^j}=\frac{1}{J}\frac{\partial}{\partial \xi^j}\left[\frac{1}{J}\left(\frac{1}{Re}+\sigma_\omega\gamma_{\text{t}}\right)b_l^j b_l^m\frac{\partial \omega}{\partial \xi^m}\right]+S_\omega \tag{7}$$

with the corresponding sources

$$S_k = \gamma_{\mathrm{t}} \frac{1}{J^2}\left(b_j^m \frac{\partial U_i}{\partial \xi^m} + b_i^m \frac{\partial U_j}{\partial \xi^m}\right)\left(b_j^n \frac{\partial U_i}{\partial \xi^n}\right) - \beta^* \omega k \tag{8}$$

$$\begin{aligned} S_\omega = {} & \gamma_{\mathrm{t}} \gamma \frac{\omega}{k} \frac{1}{J^2}\left(b_j^m \frac{\partial U_i}{\partial \xi^m} + b_i^m \frac{\partial U_j}{\partial \xi^m}\right)\left(b_j^n \frac{\partial U_i}{\partial \xi^n}\right) \\ & - \beta \omega^2 + 2(1-F_1)\sigma_{\omega 2} \frac{1}{\omega} \frac{1}{J^2}\left[\left(b_i^m \frac{\partial k}{\partial \xi^m}\right)\left(b_i^n \frac{\partial \omega}{\partial \xi^n}\right)\right] \end{aligned} \tag{9}$$

where the blending function is computed from

$$\begin{aligned} F_1 &= \tan^{-1}(\alpha_1^4) \\ \alpha_1 &= \min\left(\max\left(\frac{\sqrt{k}}{0.09\omega\delta}; \frac{1}{Re}\frac{500}{\delta^2 \omega}\right); \frac{4\sigma_{\omega 2} k}{CD_{k\omega}\delta^2}\right) \\ CD_{k\omega} &= \max\left(2\sigma_{\omega 2}\frac{1}{\omega}\frac{1}{J^2}\left(b_i^m \frac{\partial k}{\partial \xi^m}\right)\left(b_i^n \frac{\partial \omega}{\partial \xi^n}\right), 10^{-20}\right) \end{aligned} \tag{10}$$

where δ is the distance to the wall, $\beta^* = 0.09$, $\sigma_{\omega 2} = 0.856$, and $\kappa = 0.41$ are model constants, and σ_k, σ_ω, β, and $\gamma = \beta/\beta^* - \sigma_\omega \kappa^2/\sqrt{\beta^*}$ are calculated by weight averaging the k–ω and the standard k–ε models with the weight coefficient F_1. See [17] for details.

2.2. *Level set equation and reinitialization*

The level set function, as a distance function, is used to capture the free surface, where $\{\varphi = 0\}$ always corresponds to the position of the fluid interface. The sign of φ is arbitrarily set to negative in air and positive in water. The level set governing equation and reinitialization techniques are the same as those in the single-phase model [4].

2.3. *Free surface boundary conditions*

The semi-coupled method can be divided into two steps. At each time step the free surface water flow is computed first with a single-phase method assuming constant pressure and zero air stress on the interface. The second step is to compute the air flow assuming that the free surface is a moving IB. These boundary conditions on the free surface are different for water and air.

2.3.1. Water. A zero gradient boundary condition is used:

$$\nabla \mathbf{U} \cdot \vec{\mathbf{N}} = 0 \tag{11}$$

where $\vec{\mathbf{N}} = -\nabla \varphi / |\nabla \varphi|$ is the unit normal vector to the free surface. As a good approximation on the water side, the pressure can be taken as constant in the air. Also, because of Equation (11) and neglecting surface tension, the pressure jump condition is

$$\hat{p} = \frac{z}{Fr^2} \tag{12}$$

DOI: 10.1002/fld

At the free surface, zero normal gradient is used for both k and ω:

$$\nabla k \cdot \vec{\mathbf{N}} = \nabla \omega \cdot \vec{\mathbf{N}} = 0 \tag{13}$$

2.3.2. Air. Because the flow is viscous, the free surface is a moving no-slip boundary for air, and thus the jump condition for the velocity is

$$[\mathbf{U}] = 0 \tag{14}$$

The pressure at the interface is implemented by imposing the divergence-free condition for the incompressible fluid, introduced later, combined with the IB method. Similar to the situation in the water region, both k and ω are assumed to satisfy zero gradient normal to the free surface as in Equation (13).

Note that the correct boundary condition for k and ω at the free surface should be a no-slip condition, which would involve a very fine grid in the interfacial region to assure the requirement of $y^+ \sim 1$ for the first point into the air. A grid satisfying this condition in an IB approach for ship hydrodynamics problems is beyond the computational capabilities of the current machines, due to the very large Reynolds numbers present in model and full-scale problems. This is also true for two-phase surface capturing approaches. The turbulence boundary conditions in the air will affect the air velocity profile near the free surface; thus, wall functions could be used to improve the modeling of the boundary conditions on the free surface on the air side. However, forces on the air/water interface are not used in our approach (the air does not influence the water); thus, the actual turbulent boundary conditions on air side are of secondary importance and outside the scope of this paper. At the ship solid surface, where forces and moments are important, the correct boundary conditions for k and ω are imposed both in air and water.

2.4. Incoming waves

Modeling of waves is of paramount importance for seakeeping, maneuvering trajectories and survivability studies. Implementation of linear waves in water is similar to that of Carrica *et al.* [3], where initial and boundary conditions are imposed using superposition of exact potential flow solutions. Regular and irregular, unidirectional or multidirectional waves are implemented for Pierson–Moskowitz, Bretschneider, or JONSWAP spectrums [18]. The wave elevation is prescribed as

$$\xi(x, y, t) = \sum_i \sum_j a_{ij} \cos[k_i (x \cos \mu_j - y \sin \mu_j) - \omega_{e,ij} t + \phi_{ij}] \tag{15}$$

where ϕ_{ij} is a random phase, a_{ij} is the wave amplitude, $\omega_{e,ij}$ is the encounter frequency, k_i is the wavenumber, and μ_j is the angle of incidence, all for the wave component with wavelength i and angle j. The angle of incidence is composed of the dispersion angle and the heading angle α_0 of the ship, $\mu_j = \alpha_j + \alpha_0$. The encounter frequency and the wave amplitude are computed from

$$\omega_{e,ij} = k_i \cos \mu_j + \frac{1}{Fr}\sqrt{k_i} \tag{16}$$

$$a_{ij} = \sqrt{2S(\omega_i) M(\alpha_j) \delta\omega \delta\alpha} \tag{17}$$

DOI: 10.1002/fld

where the directional $M(\alpha_j)$ and frequency $S(\omega_i)$ distributions depend on the chosen spectrum. The velocities and pressure are also expressed as a superposition of potential solutions, See Carrica *et al*. [3] for a description of the implementation of a Bretschneider spectrum.

Since the water is decoupled from the air solution, no additional specification is necessary on the water side. On the air side, a velocity profile can be imposed mimicking a turbulent boundary layer [19]. This approach is considerably complex and is under development. At this point uniform air velocity is used on the far field, which causes the natural development of a boundary layer inside the computational domain.

2.5. Motions

Ship motions follow the approach described in Carrica *et al*. [2], with the additions discussed next. It should be pointed out that the grid velocity should be subtracted for the convection velocity in Equations (1), (4), (6), and (7), and in the level set transport equation (see details in [2]). This grid velocity is imposed as the no-slip boundary condition on the ship hull. To simulate moving rudders and other control surfaces or resolved propellers, a hierarchy of objects is used. The children objects (for instance the rudders) inherit the motions from the parent (the ship) and add their own motion with respect to the parent object. The rigid body equations of motion are solved in the ship coordinate system, while the fluid flow is solved in the earth coordinate system. Forces and moments are computed on the earth system, integrating separately on parent and children objects, and projected into the ship coordinate system. The motions on the children objects are defined by controller directives.

2.6. Propeller model

A prescribed body force model [20] is implemented to compute the propeller-induced velocities on the flow. This body force depends on the thrust and torque coefficients K_T and K_Q obtained from the open water curves of the propeller as a function of the advance coefficient, defined as

$$J_p = \frac{U}{n D_p} \tag{18}$$

where n is the angular velocity of the propeller, D_p is the propeller diameter and U is the velocity the propeller location, approximated in this work as the ship forward velocity.

2.7. Controllers

Active and passive controllers have been implemented. Controllers offer a flexible way of imposing simple maneuvers, replicating experimental conditions, and analyzing the ship performance under different situations. Controllers impose a variety of ramps in ship forward speed and propeller rotational speed, turning and zig-zag maneuvers, proportional integral derivative (PID) speed control (controlling a propeller body force model or a fully modeled rotating propeller), PID heading control (controlling rudder angle), PID autopilot (using simultaneously speed and heading control), and waypoint control (using autopilot with variable heading).

The controllers are either logical, based on on/off signals and limiting action parameters, or active PID type. Limiters of action use physical limits of the actuators to add reality to the resulting actuator setting. For instance, a rudder has a maximum and minimum operational angle, and a maximum allowed rudder rate. PID controllers use the classical action law

$$\frac{\mathrm{d}\phi}{\mathrm{d}t}=Pe+I\int_0^t e\,\mathrm{d}t+D\frac{\mathrm{d}e}{\mathrm{d}t} \tag{19}$$

where ϕ is an action parameter; for instance, the rudder angle, and e is the error of the controlled value with respect to the target value (for instance, heading with respect to desired heading), given by

$$e=\psi-\psi_{\mathrm{target}} \tag{20}$$

For the autopilot model of this work proportional derivative (PD) controllers are used. For the speed velocity, the controller acts on the rotational speed of the propellers following the law

$$\frac{\mathrm{d}n}{\mathrm{d}t}=Pe_U+D\frac{\mathrm{d}e_U}{\mathrm{d}t} \tag{21}$$

with the error defined as $e_U=U_{\mathrm{ship}}-U_{\mathrm{target}}$. The heading is controlled by acting on the rudder angle as

$$\frac{\mathrm{d}\delta}{\mathrm{d}t}=Pe_\psi+D\frac{\mathrm{d}e_\psi}{\mathrm{d}t} \tag{22}$$

with the error in heading defined in Equation (20).

The PID controller parameters are constant throughout the computation.

3. NUMERICAL METHODS

The semi-coupled method was implemented into the code CFDShip-Iowa v4.0, a body-fitted coordinate parallel CFD code originally based on the single-phase level set method [2–4, 21]. A schematic of the solution strategy is shown in Figure 1. The flow in water is solved first using the same numerical methods described in Carrica *et al.* [3, 4], with a fully implicit predictor–corrector for the motions [2], but updating only the forces in water and leaving the forces in air lagging from the previous time step. This implicit-in-water/explicit-in-air approach can be justified in view of the fact that air forces amount typically to 1% or less of the total force (see computational examples). Once the water flow is known the air flow is solved. Note that on convergence of the air flow, the predictor step for the motions uses the latest forces in air and water.

The main numerical methods used to solve the air flow in the semi-coupled method are presented next, most of them inherited from CFDShip-Iowa v4.0, as the semi-coupled air/water method builds on the same ideas. New implementations related with the solution of the air flow are discussed in detail.

3.1. Discretization strategy

Second-order Euler backward differences are used for the time derivatives of all variables. For an arbitrary variable ϕ

$$\frac{\partial\phi}{\partial\tau}=\frac{1}{\Delta\tau}(1.5\varphi^n-2\phi^{n-1}+0.5\phi^{n-2}) \tag{23}$$

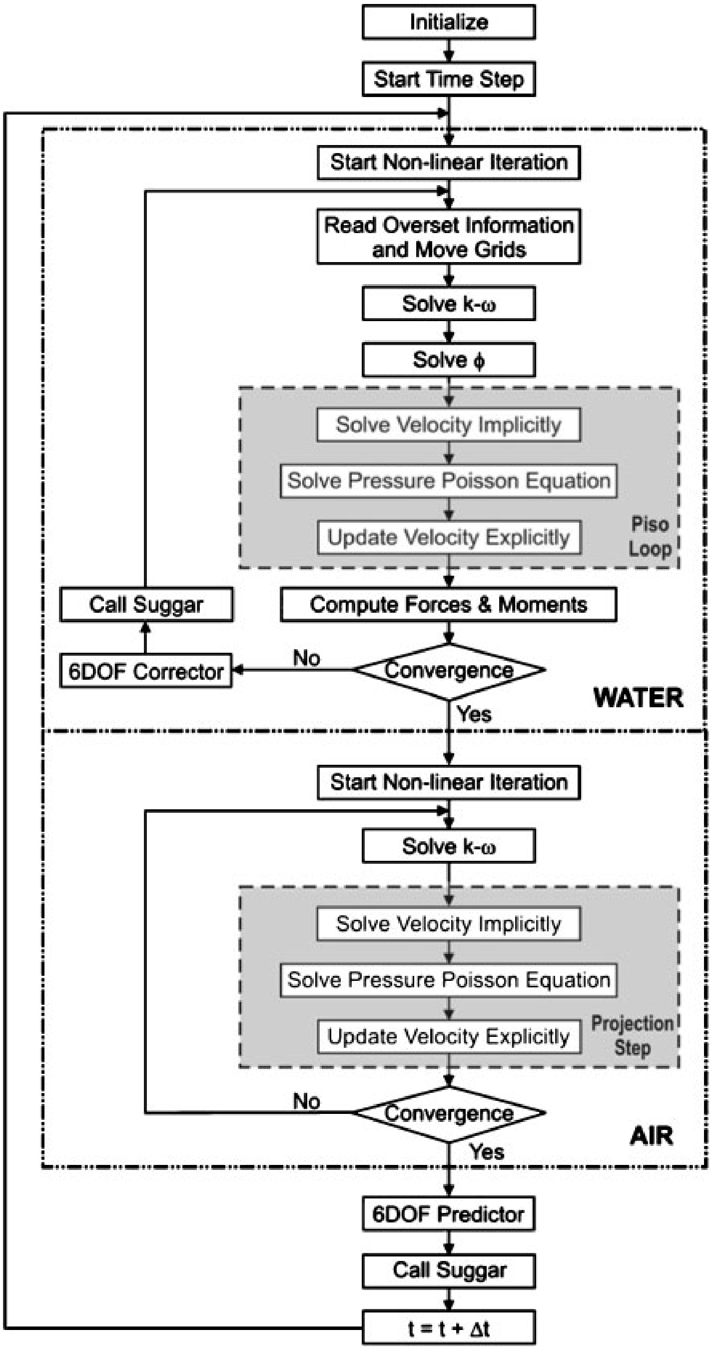

Figure 1. Solution strategy.

The convective terms are discretized with a second-order upwind method. Although a second-order upwind suffers from phase errors, it is more robust than more accurate higher-order methods, especially in the cases with very large density ratio in regions of sub-optimal grid quality. Taking an arbitrary control volume P on the computational domain, the convection terms for an arbitrary variable ϕ can be expressed as

$$\frac{1}{J}\frac{\partial}{\partial \xi^j}(\breve{U}^j\phi)=\frac{1}{J}[(C_\mathrm{d}\phi_\mathrm{d}-C_\mathrm{u}\phi_\mathrm{u})+(C_\mathrm{e}\phi_\mathrm{e}-C_\mathrm{w}\phi_\mathrm{w})+(C_\mathrm{n}\phi_\mathrm{n}-C_\mathrm{s}\phi_\mathrm{s})] \tag{24}$$

where u, d, w, e, s, and n stand for the up $(i-\frac{1}{2})$, down $(i+\frac{1}{2})$, west $(j-\frac{1}{2})$, east $(j+\frac{1}{2})$, south $(k-\frac{1}{2})$, and north $(k+\frac{1}{2})$ faces of the control volume, respectively. For example, at the down face

$$c_\mathrm{d}=(\breve{U}^1)_\mathrm{d} \tag{25}$$

$$C_\mathrm{d}\phi_\mathrm{d}=\max(c_\mathrm{d},0)\phi_\mathrm{d}^+-\max(-c_\mathrm{d},0)\phi_\mathrm{d}^- \tag{26}$$

$$\phi_\mathrm{d}^+=1.5\phi_i-0.5\phi_{i-1} \tag{27}$$

$$\phi_\mathrm{d}^-=1.5\phi_{i+1}-0.5\phi_{i+2} \tag{28}$$

Note that the contravariant velocity in Equation (25) has to be evaluated at the cell face, which is done by linear interpolation of the node values. The metrics are computed directly at the half-cell location so as to avoid spurious sources in the evaluation of the divergence. The described convective discretization is applied for all the convective terms, including the momentum, turbulence, and level set equations.

The viscous terms in the momentum and turbulence equations are computed with a second-order central difference scheme. For an arbitrary variable ϕ, the diffusive term can be expressed as

$$\frac{1}{J}\frac{\partial}{\partial \xi^j}\left(\frac{a^{jk}}{Re_\mathrm{eff}}\frac{\partial \phi}{\partial \xi^k}\right)=D_\mathrm{d}-D_\mathrm{u}+D_\mathrm{e}-D_\mathrm{w}+D_\mathrm{n}-D_\mathrm{s} \tag{29}$$

where $a^{jk}=b_l^j b_l^k/J$, and the diffusive flux in the down direction is

$$D_\mathrm{d}=\frac{1}{J_\mathrm{d}}\left(\frac{a^{1k}}{Re_\mathrm{eff}}\frac{\partial \phi}{\partial \xi^k}\right)_\mathrm{d} \tag{30}$$

Other directions are dealt with similarly. The discretization of Equation (29) leads to a 19-point stencil.

After discretization, the momentum equation takes the algebraic form

$$a_P U_i^n+\sum_\mathrm{nb} a_\mathrm{nb} U_{i,\mathrm{nb}}^n=s_{U_i}-\frac{1}{J}b_i^l\frac{\partial \hat{p}^n}{\partial \xi^l} \tag{31}$$

where a_P is the pivot and a_nb are the neighbor coefficients, respectively. s_{U_i} is the source term including the variables from the previous time step arising from Equation (23), cross-derivative terms, and source term of the momentum equation. n represents the nonlinear iteration. The transport velocity is the latest available and causes the system to be non-linear. Other sources of non-linearity include free-surface and object motions and non-linear turbulence equations.

Equation (31) is solved at all points in air. Points in water are used to define the no-slip free surface boundary condition for air, which in an immerse boundary sense means that the velocities in water can be used directly to compute the air flow. At all points in water, Equation (31) is modified as

$$a_P U_i^n + \sum_{\mathrm{nb}} a_{\mathrm{nb}} U_{i,\mathrm{nb}}^n = s_{U_i} \tag{32}$$

where $a_P = 1$, $a_{\mathrm{nb}} = 0$, $s_{U_i} = (U_i^n)_{\mathrm{water}}$.

3.2. *Pressure Poisson equation*

A projection algorithm [22] is used to satisfy mass conservation in air. The momentum equation, Equation (1), can be expressed as

$$\frac{\partial \mathbf{U}}{\partial \tau} + \nabla \hat{p} = \mathbf{V} \tag{33}$$

where $\mathbf{V}$ is a differential expression of $\mathbf{U}$ representing the rest of the terms in the momentum equation not explicitly shown in Equation (33). Taking the divergence of Equation (33) and noting that $\nabla \cdot (\partial \mathbf{U}/\partial \tau) = 0$,

$$\nabla \cdot \nabla \hat{p} = \nabla \cdot \mathbf{V} \tag{34}$$

Equation (34) is a Poisson equation for the pressure. The resulting pressure is used to explicitly update the velocity field by solving

$$\frac{\partial \mathbf{U}}{\partial \tau} = \mathbf{P}(\mathbf{V}) = \mathbf{V} - \nabla \hat{p} \tag{35}$$

where $\mathbf{P}(\mathbf{V})$ is the projection vector. Details of the discrete form of Equations (33)–(35) are important and are discussed next. At the current time n, $\mathbf{V}$ is computed from the left-hand side of Equation (33) using an estimated value $\mathbf{U}^{*k}$, which is the latest available velocity vector,

$$\mathbf{V} = \frac{1}{\Delta \tau}(1.5\mathbf{U}^{*,k} - 2\mathbf{U}^{n-1} + 0.5\mathbf{U}^{n-2}) + \nabla \hat{p}^{n,k} \tag{36}$$

Let the projection vector be

$$\mathbf{P}(\mathbf{V}) = \mathbf{V}_{\mathrm{d}} = \frac{1}{\Delta \tau}(1.5\mathbf{U}^{n,k+1} - 2\mathbf{U}^{n-1} + 0.5\mathbf{U}^{n-2}) \tag{37}$$

introducing Equation (33)

$$\mathbf{V}_{\mathrm{d}} + \nabla \hat{p}^{n,k+1} = \mathbf{V} \tag{38}$$

and Equation (34) has the form

$$\nabla \cdot (\nabla \hat{p}^{n,k+1}) = \nabla \cdot \mathbf{V} \tag{39}$$

After solving Equation (39) for the pressure, the projection vector is obtained:

$$\mathbf{V}_{\mathrm{d}} = \mathbf{V} - \nabla \hat{p}^{n,k+1} \tag{40}$$

and the updated velocity can then be expressed as

$$\mathbf{U}^{n,k+1}=\mathbf{U}^{*,k}+\frac{\Delta\tau}{1.5}(\nabla\hat{p}^{n,k}-\nabla\hat{p}^{n,k+1}) \tag{41}$$

In our implicit scheme, Picard iterations are used to converge the non-linear convective term in the momentum equations. The updated velocity obtained from Equation (41) is substituted into Equation (31), and a new velocity is obtained. This way the pressure and velocity are iterated to convergence. The Poisson Equation (39) in curvilinear grids is expressed as

$$\frac{\partial}{\partial\xi^j}\left(E^{jl}\frac{\partial\hat{p}}{\partial\xi^l}\right)=\hat{d} \tag{42}$$

where $\hat{p}^{n,k+1}$ was replaced by $\hat{p}$, and

$$E^{jl}=\frac{b_i^j b_i^l}{J} \tag{43}$$

$$\hat{d}=\breve{V}_{\mathrm{d}}^1-\breve{V}_{\mathrm{u}}^1+\breve{V}_{\mathrm{e}}^2-\breve{V}_{\mathrm{w}}^2+\breve{V}_{\mathrm{n}}^3-\breve{V}_{\mathrm{s}}^3 \tag{44}$$

The contravariant velocities at the cell faces are computed by averaging. For instance, at the down face

$$\breve{V}_{\mathrm{d}}^1=(b_l^1)_{i+1/2}\frac{V_{l,i}+V_{l,i+1}}{2} \tag{45}$$

The contravariant pressure gradient is expressed as

$$\breve{\nabla}\hat{p}^j=E^{jl}\frac{\partial\hat{p}}{\partial\xi^l} \tag{46}$$

and computing the divergence similarly to Equation (44) results in

$$\breve{\nabla}\hat{p}_{\mathrm{d}}^1-\breve{\nabla}\hat{p}_{\mathrm{u}}^1+\breve{\nabla}\hat{p}_{\mathrm{e}}^2-\breve{\nabla}\hat{p}_{\mathrm{w}}^2+\breve{\nabla}\hat{p}_{\mathrm{n}}^3-\breve{\nabla}\hat{p}_{\mathrm{s}}^3=\hat{d} \tag{47}$$

To guarantee a strong pressure/velocity coupling, discretization of the contravariant pressure gradients is made on the cell faces. For example,

$$\begin{aligned}\breve{\nabla}\hat{p}_{\mathrm{d}}^1 &= E_{i+1/2}^{11}(\hat{p}_{i+1,j,k}-\hat{p}_{i,j,k})\\ &\quad+\frac{E_{i+1/2}^{12}}{4}(\hat{p}_{i,j+1,k}-\hat{p}_{i,j-1,k}+\hat{p}_{i+1,j+1,k}-\hat{p}_{i+1,j-1,k})\\ &\quad+\frac{E_{i+1/2}^{13}}{4}(\hat{p}_{i,j,k+1}-\hat{p}_{i,j,k-1}+\hat{p}_{i+1,j,k+1}-\hat{p}_{i+1,j,k-1})\end{aligned} \tag{48}$$

Curvilinear coordinates lead to a 19-point stencil for the pressure equation. The discrete form of Equation (47) is

$$a_P\hat{p}_P+\sum_{\mathrm{nb}=1}^{18}a_{\mathrm{nb}}\hat{p}_{\mathrm{nb}}=b \tag{49}$$

where a_p is the diagonal component of the pressure matrix, a_{nb} are the off-diagonal coefficients, and b is the right-hand side term.

3.3. *IB method for curvilinear grids*

Because the free surface is immersed in the curvilinear grid, it can be regarded as a moving IB, where appropriate velocity and pressure boundary conditions should be enforced. The IB method [13, 14], traditionally used in Cartesian grids, is extended to body-fitted curvilinear grids. As discussed in the previous section, the velocity at grid points in the water region can be used directly while solving the momentum equations in the air region. However, a pressure boundary condition cannot be imposed on the free surface directly. This difficulty can be overcome by enforcing the divergence-free condition at the free surface. Ghost pressures are adopted at all grids points that are first neighbors to the interface in the water region (named IB points), including fringe points arising from overset grids. This approach makes the computation very stable because the forcing points in the air region close to the IB can be computed and corrected under a sharp interface condition.

3.3.1. Divergence-free condition at IB points. The contravariant velocity is obtained after multiplying by the adjugate Jacobian matrix in Equation (40)

$$\breve{U}^i = \breve{V}^i - E^{ij}\frac{\partial \phi}{\partial \xi^j} \tag{50}$$

where $\breve{U}^i = b^i_l V^{n,k+1}_{\mathrm{d},l}$, $\breve{V}^i = b^i_l V^{n,k+1}_l$, and $\phi = p^{n,k+1}$. In an orthogonal or nearly orthogonal grid E^{ij} can be approximated by E^{ii}, neglecting the cross terms. Thus,

$$\breve{U}^i = \breve{V}^i - E^{ii}\frac{\partial \phi}{\partial \xi^i} \tag{51}$$

$$E^{ii} = \frac{b^i_l b^i_l}{J} \tag{52}$$

The divergence-free condition is expressed as

$$\breve{U}^1_{\mathrm{d}} - \breve{U}^1_{\mathrm{u}} + \breve{U}^2_{\mathrm{e}} - \breve{U}^2_{\mathrm{w}} + \breve{U}^3_{\mathrm{n}} - \breve{U}^3_{\mathrm{s}} = 0 \tag{53}$$

3.3.2. Pressure equation for case 1: only one neighbor point in air. For a point P in water with a neighbor in air D (see Figure 2(a)), the divergence-free condition can be expressed as

$$\frac{(\breve{U}^1_{\mathrm{d}} - \breve{U}^1_P)}{0.5} + \breve{U}^2_{\mathrm{e}} - \breve{U}^2_{\mathrm{w}} + \breve{U}^3_{\mathrm{n}} - \breve{U}^3_{\mathrm{s}} = 0 \tag{54}$$

If an arithmetic average for the face velocity $\breve{U}^1_{\mathrm{d}} = 0.5(\breve{U}^1_P + \breve{U}^1_D)$ is used, Equation (53) becomes

$$\breve{U}^1_D - \breve{U}^1_P + \breve{U}^2_{\mathrm{e}} - \breve{U}^2_{\mathrm{w}} + \breve{U}^3_{\mathrm{n}} - \breve{U}^3_{\mathrm{s}} = 0 \tag{55}$$

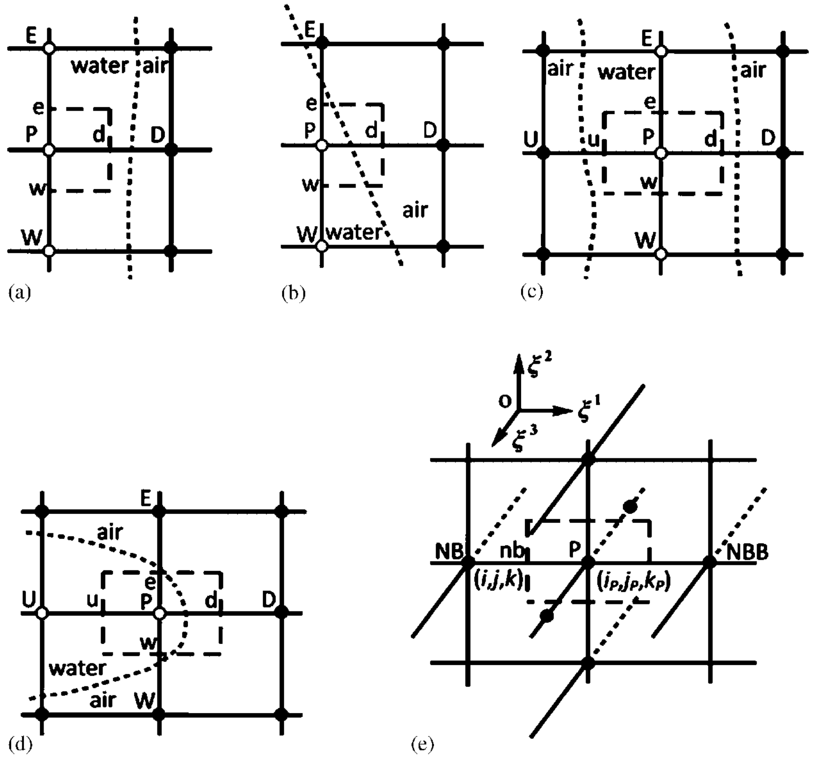

Figure 2. Schematic view of a grid near the interface in the computational domain: (a) one neighbor point in the air; (b) two neighbor points in the different coordinates; (c) two neighbor points in the same coordinates; (d) three neighbor points in the air; and (e) general case for IB point P.

From Equation (51) results

$$\breve{U}^1_D = \breve{V}^1_D - (E^{11})_D \left(\frac{\partial \phi}{\partial \xi^i}\right)_D \tag{56}$$

and using the following approximations:

$$\left(\frac{\partial \phi}{\partial \xi^i}\right)_D = \phi_D - \phi_P, \quad (E^{11})_D \approx (E^{11})_{\mathrm{d}} \tag{57}$$

then

$$\breve{U}^1_D = \breve{V}^1_D - (E^{11})_{\mathrm{d}} (\phi_D - \phi_P) \tag{58}$$

Finally,

$$(E^{11})_{\mathrm{d}} (\phi_D - \phi_P) = \breve{V}^1_D - \breve{U}^1_P + \breve{U}^2_{\mathrm{e}} - \breve{U}^2_{\mathrm{w}} + \breve{U}^3_{\mathrm{n}} - \breve{U}^3_{\mathrm{s}} \tag{59}$$

In the above equation, $\breve{U}^1_P, \breve{U}^2_{\mathrm{e}}, \breve{U}^2_{\mathrm{w}}, \breve{U}^3_{\mathrm{n}}$, and $\breve{U}^3_{\mathrm{s}}$ are given from the water solution, and $\breve{V}^1_D$ is obtained from the air side; thus, ϕ_P and ϕ_D are coupled explicitly.

3.3.3. *Pressure equation for case 2: Two neighbor points in the air.*

3.3.3.1. Two points in the different coordinates. From Figure 2(b), it can be seen that there are two neighbor points D and E in air, located in different coordinates.

As before, the divergence-free condition at point P is as follows:

$$\frac{(\breve{U}_{\mathrm{d}}^1-\breve{U}_P^1)}{0.5}+\frac{(\breve{U}_{\mathrm{e}}^2-\breve{U}_P^2)}{0.5}+\breve{U}_{\mathrm{n}}^3-\breve{U}_{\mathrm{s}}^3=0 \tag{60}$$

and following the procedure of case 1 yields

$$(E^{11})_{\mathrm{d}}(\phi_D-\phi_P)+(E^{22})_{\mathrm{e}}(\phi_E-\phi_P)=\breve{V}_D^1-\breve{U}_P^1+\breve{V}_E^2-\breve{U}_P^2+\breve{U}_{\mathrm{n}}^3-\breve{U}_{\mathrm{s}}^3 \tag{61}$$

3.3.3.2. Two points in the same coordinate. From Figure 2(c), two neighbor points U and D are in air, located in same coordinate. The divergence-free condition at point P is as follows:

$$0.5(\breve{U}_D^1-\breve{U}_U^1)+\breve{U}_{\mathrm{e}}^2-\breve{U}_{\mathrm{w}}^2+\breve{U}_{\mathrm{n}}^3-\breve{U}_{\mathrm{s}}^3=0 \tag{62}$$

Then, the pressure equation is as follows:

$$0.5(E^{11})_{\mathrm{d}}(\phi_D-\phi_P)+0.5(E^{11})_{\mathrm{u}}(\phi_U-\phi_P)=0.5(\breve{V}_D^1-\breve{V}_U^1)+(U_{\mathrm{e}}^2-\breve{U}_{\mathrm{w}}^2)+(U_{\mathrm{n}}^3-\breve{U}_{\mathrm{s}}^3) \tag{63}$$

3.3.4. Pressure equation for case 3: three neighbor points in the air. In the case of Figure 2(d) there are three neighbor points W, D, and E in air. The divergence-free condition at point P is then

$$\frac{(\breve{U}_{\mathrm{d}}^1-\breve{U}_P^1)}{0.5}+0.5(\breve{U}_E^2-\breve{U}_W^2)+\breve{U}_{\mathrm{n}}^3-\breve{U}_{\mathrm{s}}^3=0 \tag{64}$$

Then, the pressure equation is as follows:

$$\begin{aligned}(E^{11})_{\mathrm{d}}(\phi_D-\phi_P)&+0.5(E^{22})_{\mathrm{e}}(\phi_E-\phi_P)+0.5(E^{22})_{\mathrm{w}}(\phi_W-\phi_P)\\&=(\breve{V}_D^1-\breve{U}_P^1)+0.5(\breve{V}_E^2-\breve{V}_W^2)+(\breve{U}_{\mathrm{n}}^3-\breve{U}_{\mathrm{s}}^3)\end{aligned} \tag{65}$$

Other directions or cases with more neighbors in air are treated similarly.

3.3.5. Pressure equation for the general three-dimensional case. In general, the discretized Poisson equation from Equation (53) for an arbitrary IB point P can be expressed as

$$\mathrm{LHS}=\mathrm{RHS} \tag{66}$$

where LHS and RHS are the left-hand side and right-hand side of the Poisson equation, respectively. Let NB be one of six neighbor points to P, nb the control volume face point between NB and P, and NBB is the other neighbor of P along the same gird line NB–P (see Figure 2(e)). P and NB coordinates are (i_P, j_P, k_P) and (i, j, k), respectively. NBB is thus at $(2i_P-i, 2j_P-j, 2k_P-k)$. The position shift of NB with respect to P is computed from $(i', j', k')=(i-i_P, j-j_P, k-k_P)$, and the sign of the shift is $\mathrm{sign(NB)}=i'+j'+k'$. The gridline coordinate is $n=|i'|+2|j'|+3|k'|$ (n is either 1, 2, or 3). Initialization is then performed as $\mathrm{LHS}=\mathrm{RHS}=0$. There are only four possible combinations for points NB and NBB depending whether they are in the water or air. The resulting correction relations for the pressure matrix are:

(1) NB is in air and NBB is in water:

$$\mathrm{LHS}=\mathrm{LHS}+\{0.5(E^{nn})_{\mathrm{nb}}(\phi_{\mathrm{NB}}-\phi_P)\}/0.5 \tag{67}$$

$$\mathrm{RHS}=\mathrm{RHS}+\mathrm{sign}(\mathrm{NB})\{0.5(\breve{V}^n_{\mathrm{NB}}+\breve{U}^n_P)\}/0.5 \tag{68}$$

(2) NB is in water and NBB is in air:

$$\mathrm{LHS}=\mathrm{LHS}+0 \tag{69}$$

$$\mathrm{RHS}=\mathrm{RHS}+\mathrm{sign}(\mathrm{NB})\breve{U}^n_P/0.5 \tag{70}$$

(3) Both points are in air:

$$\mathrm{LHS}=\mathrm{LHS}+\{0.5(E^{nn})_{\mathrm{nb}}(\phi_{\mathrm{NB}}-\phi_P)\} \tag{71}$$

$$\mathrm{RHS}=\mathrm{RHS}+\mathrm{sign}(\mathrm{NB})\{0.5(\breve{V}^n_{\mathrm{NB}}+\breve{U}^n_P)\} \tag{72}$$

(4) Both points are in water:

$$\mathrm{LHS}=\mathrm{LHS}+0 \tag{73}$$

$$\mathrm{RHS}=\mathrm{RHS}+\mathrm{sign}(\mathrm{NB})\breve{U}^n_{\mathrm{nb}} \tag{74}$$

This procedure is applied to all six neighbor points NB, yielding the discretized three-dimensional Poisson equation at point P. In addition, a divergence-free condition is used to derive the Poisson equation at the grid points on the wall, following the same procedure reported in [2], which accounts for wall and grid velocities. This treatment is compatible to the treatment of IB points introduced above. Note that the velocity is imposed at the neighbor point in water and not on the interface itself. It should also be pointed out that a 19-point stencil is still used to discretize the pressure equation for all points in air. A problem may arise when a point in air has cross points that are in water (for instance i, j, k is in air and $i+1, j+1, k$ is in water) and that point is not first neighbor to any point in air. Since the point in water does not have a neighbor in air at any of the faces of the control volume, no pressure equations can be written there. For those cases the pressure values are simply copied from the air points into the water points. In nearly orthogonal grids, this will not cause a big problem, since the cross-term coefficients will be small.

3.4. Dynamic overset grids

The overset implementation is similar to that of the single-phase solver [4, 21], with the difference that the pressure at the ghost points in water neighbor to the free surface is solved by imposing continuity even if they are fringe points. This is done following the procedure described in the previous section.

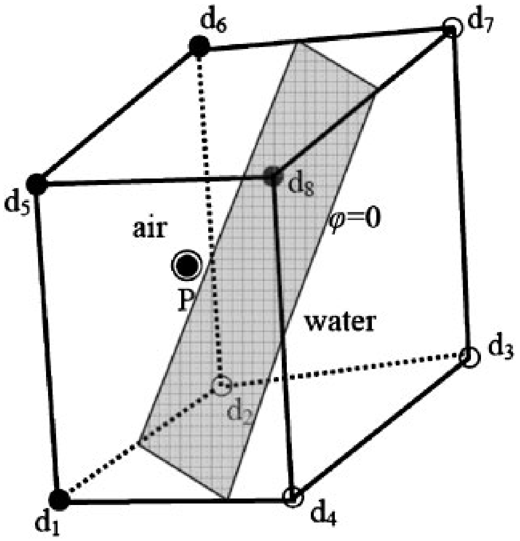

Figure 3. Donor cell with grid points in the water.

The pressure at the fringe points in the air region is interpolated from the donor points. If all eight points in the donor cell are in the air region, then the pressure at the fringe point can be expressed as (referring to Figure 3)

$$\phi_P = -\sum_{\mathrm{id}=1}^{8} \alpha_{\mathrm{id}} \phi_{\mathrm{id}} \tag{75}$$

where α_{id} is the interpolation coefficient and id sweeps over eight donor points associated with point *P*. However, if the pressure at a donor point is unknown (for example, point 3 in Figure 3, which is in water and is not first neighbor to any air point, as the discussion in the previous section), then a zero gradient condition is enforced; hence, Equation (75) is expressed as

$$(1+\alpha_3)\phi_P = -\sum_{\mathrm{id}=1}^{2} \alpha_{\mathrm{id}} \phi_{\mathrm{id}} - \sum_{\mathrm{id}=4}^{8} \alpha_{\mathrm{id}} \phi_{\mathrm{id}} \tag{76}$$

3.5. Treatment of bubbles

Since the method is semi-coupled, pressure is not transferred from air to water or *vice versa*. Water simply ignores the presence of air, while air sees water as a no-slip boundary and thus the resulting pressure condition after enforcing continuity is of the Neumann type. Air obtains its reference pressure from the far-field boundaries, where the pressure is set to atmospheric. When a bubble forms, the air is disconnected from the Dirichlet condition on the far field and the pressure is undefined. To avoid this problem, bubbles are collapsed by changing the grid points in air to water.

4. COMPUTATION EXAMPLES

A series of tests was performed to evaluate implementation of the wind over waves and the performance and robustness of the proposed method to compute complex ship flows.

4.1. Laminar Couette flow over a wavy boundary

In order to validate the semi-coupled model and method, a two-dimensional laminar Couette flow over a stationary wavy boundary is simulated first, as studied by Benjamin [23]; see Figure 4. Benjamin [23] investigated several variants of this idealized flow theoretically and provided closed-form solutions for surface pressure and shear stress under the restrictions of small wave slope, zero phase speed, high Reynolds number, and linear velocity profiles. These analytical solutions provide a convenient benchmark for model and code.

The solution provided by Benjamin [23] for the non-dimensional pressure at the boundary is

$$\hat{p} = -0.776ak^{-1/3}\,Re^{-1/3}G^{5/3}\{\cos(k\xi-\pi/6)+0.776\alpha\cos(k\xi-\pi/3)\} \tag{77}$$

and the non-dimensional shear stress is

$$\hat{\tau} = 1.065ak^{1/3}Re^{-2/3}G^{4/3}\{\cos(k\xi+\pi/6)+0.776\alpha\cos k\xi\} \tag{78}$$

where a is the wave amplitude, $k=2\pi/\lambda$ is the wave number, λ is the wavelength, the velocity gradient along vertical direction G is constant, $\alpha = k/(k\,Re\,G)^{1/3}$, and ξ is the curvilinear coordinate

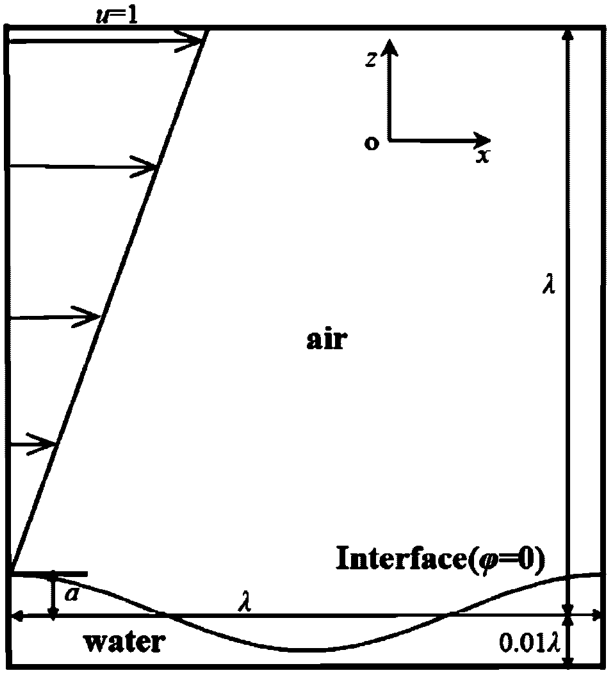

Figure 4. Sketch of Couette flow and computational domain in one wavelength.

along the bottom boundary, which is approximately equal to x when the wave slope is small. The case has also been simulated by Sullivan *et al.* [19] using a body-fitted approach, with wave slope $ak=0.01$, phase speed $c=0$, $Re=10^4$, and $G=1$. The computation domain is $(L_x, L_z)=(\lambda, 1.01\lambda)$ (see Figure 4), with periodic boundary conditions on the inlet and outlet boundaries. The same case was computed using a coarse grid ($30\times5\times45$), where five points are set along the y-coordinate for our three-dimensional code, a uniform spacing is used in the axial x-coordinate, and clustering is used in the vertical z-coordinate to resolve the flow near the IB. At this location, a grid spacing of 3.34×10^{-4} is used ($y^+=1$ corresponds to $\Delta z=0.01$) with 13 grid points inside the wavy boundary. This grid is finer than that used by Sullivan *et al.* [19] near the bottom boundary, because it is an IB and does not exactly conform to the curved geometry. For the fine grid $120\times5\times181$ grid points are used, with a refinement ratio of 4 with respect to the coarse grid.

In Figure 5, computational results are compared with the analytical solution for the normalized surface pressure $\hat{p}/aku^{*2}$ and normalized shear stress τ/u^{*2} (note that $\tau/u^{*2}=\hat{\tau}/u^{*2}+1$) along the streamline direction, where the wave slope $ak=0.01$, and $u^*=(\tau_w/\rho_a U_0^2)^{1/2}$ is the wall friction velocity based on the constant total stress τ_w. From Figure 5(a), it can be seen that for the coarse grid both pressure and shear stress agree well with the analytical solutions, showing an agreement similar to the results by Sullivan *et al.* [19]. The phase and amplitude are faithfully captured by the numerical solution both for pressure and stress. The finer grid gives an even closer agreement, as shown in Figure 5(b). This suggests that the method properly converges to the analytical solution as the grids are refined.

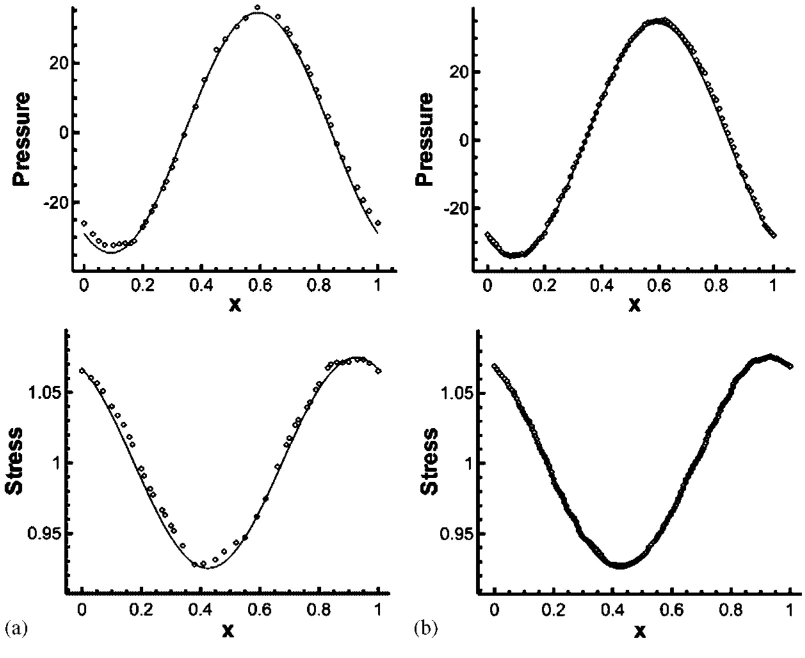

Figure 5. Comparison of normalized surface pressure and shear stress with analytical solution (lines) and numerical results (symbols) for two-dimensional laminar Couette flow on a wavy surface: (a) coarse and (b) fine grid.

4.2. Free surface flow around a surface combatant

The problem under study is a U.S. Navy surface combatant restrained from motions, advancing in calm water with sinkage and trim fixed at the dynamic condition. The ship is the bare hull DTMB model 5512, a 1:46.6 model scale of a modern surface combatant. The geometry is a benchmark on the ship hydrodynamics community, tested in the towing tanks at DTMB, IIHR (Iowa), and INSEAN (Italy), and selected as test case for code validation at the Ship Hydrodynamics CFD workshops in Gothenburg, 2000 [24], and Tokyo, 2005 [25]. Numerical results are compared and validated in this work against the data taken at the IIHR towing tank by Gui *et al.* [26], and Longo and Stern [27].

The simulation is performed at medium speed, corresponding to a Froude numbers $Fr=0.28$, and Reynolds numbers of $Re_{\mathrm{w}}=4.85\times 10^6$ in water and $Re_{\mathrm{a}}=3.23\times 10^5$ in air. This computation was also performed under the same conditions with a two-phase level set method by Huang *et al.* [12]. Air/water density and viscosity ratios are 1.2×10^{-3} and 1.8×10^{-2}, respectively.

A double-O topology grid was generated with a hyperbolic solver. A slightly curved bare deck was added to analyze the air flow. The domain extents are $-0.7<x<2$, $0<y<1$, $-1<z<0.6$. The total number of grid points was 615 000, distributed in 16 blocks for parallel processing. Since the problem is symmetric, only half the ship was computed and symmetry boundary conditions used. The whole far field was set to inlet boundary condition, while no-slip was used at the ship hull. The grid spacing on the first grid point away from the wall was set such that $y^+<1$.

Figures 6 and 7 show the time history of the resistance coefficient in the water and air regions, respectively, defined as

$$C_T=\frac{F_x}{(1/2)\rho_l U_0^2 A_{\mathrm{s}}} \tag{79}$$

where A_{s} is the static wetted area of the ship. The resistance coefficient was computed integrating forces over the no-slip surfaces separately in water and air. After some time needed to develop the Kelvin waves and the ship's boundary layer, the force coefficients converge to a steady-state value both in the water and air regions. The final resistance coefficient, shown in Table I, is around 5.4% higher than the experimental value measured in the water region. These differences are within

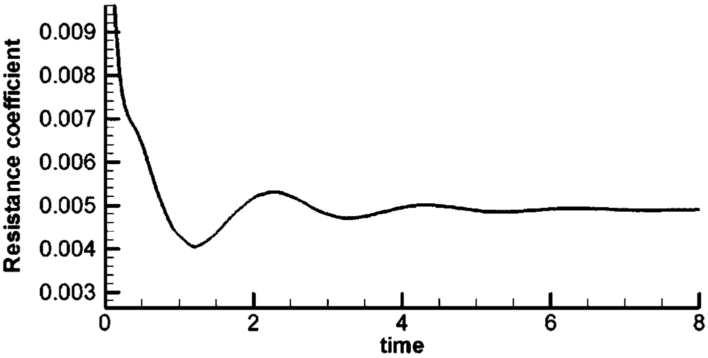

Figure 6. Convergence history of the resistance coefficient in water.

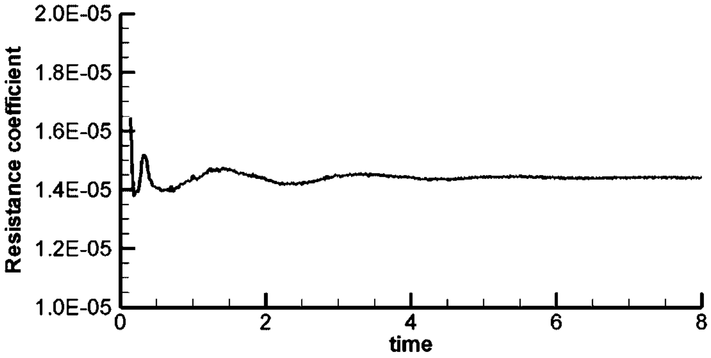

Figure 7. Convergence history of the resistance coefficient in air.

Table I. CFD predictions of resistance and comparison with EFD results.

CFD Air/water	Total (EFD)	Total (CFD)	$\frac{\text{CFD}-\text{EFD}}{\text{EFD}}$ (%)
0.000015/0.00486	0.00461	0.00486	5.4

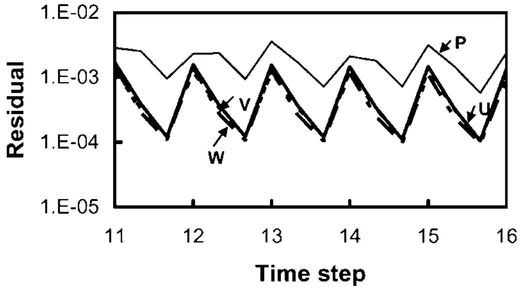

Figure 8. Typical convergence history of the non-linear iterations of air flow.

typical values for RANS resistance computations. Figure 8 shows the typical convergence history of the non-linear Picard iterations from time 0.1 to 0.15 (time step = 11–15, $Fr = 0.28$), where the ship is in a strong acceleration transient. The non-linear iterations are limited to a minimum of 3 or stopped when the residual decreases to 10^{-3} for all variables. At a later stage, when close to the steady-state solution, the solution changes little between time steps, and the number of non-linear iterations reduces to typically 3.

The air/water interface elevation compared with experimental data for $Fr = 0.28$ is shown in Figure 9. The numerical results compare very well with the experimental values near the hull. Farther out the Kelvin wave is diffused, as expected for this relatively coarse double-O grid. It must also be stressed that a significant number of the grid points are used to resolve the air flow, and thus the grid used in water can be considered coarse.

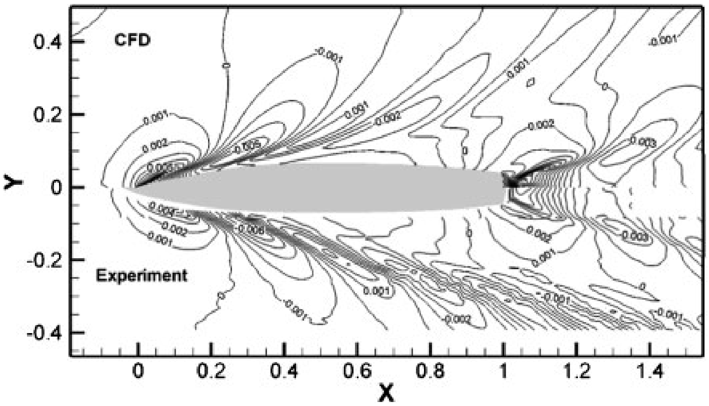

Figure 9. Wave elevation (5512, $Fr=0.28$).

Experimental particle image velocimetry measurements of the three-dimensional velocity field at the propeller plane $x=0.935$ (the nominal wake) have been reported by Gui *et al.* [26], and Longo and Stern [27]. Huang *et al.* [12] compared their computational results of the fully coupled two-phase method with the experimental data, showing good agreement although EFD data are available only in the water region. Similarly, CFD results are compared with EFD data in the water region. As shown in Figure 10(a)–(c), the axial, transverse, and vertical velocities have excellent agreement with the experimental data. In addition, the air flow is compared against a fully coupled method. Figure 10(d) shows the axial velocity contours at the nominal wake plane for both the semi-coupled and fully coupled methods, showing good agreement. Both methods capture the bulging of the boundary layer caused by an interaction between the sonar dome tip vortex and the boundary layer. The velocity contours in air are very similar. A momentum defect is also observed in the air, caused by a vortex detached from the bow in the air and its interaction with the air boundary layer. This deck edge vortex has been observed on computations for frigates and carriers and can cause instabilities detrimental to safe aircraft landings.

The transversal and vertical velocities in the nominal wake plane are shown in Figure 10(e), (f). It can be seen that the results of semi-coupled method have excellent agreement with the fully coupled solutions; the air wake structures and the velocity magnitudes are basically very close. In addition, note the good level of continuity of the velocity field across the air/water interface for all components of the velocity. However, there are some small differences in the velocity contours near the free surface. The velocities are smoother under for the two-phase fully coupled method, which can be expected since the jump conditions across the interface are explicitly enforced.

It is interesting to compare the total computational time and time step requirements for the fully- and semi-coupled methods. In both cases the simulation time is 8 dimensionless seconds (the ship advances 8 ship lengths). The fully coupled method requires a time step of 0.0005 for a total of 16 000 time steps, while the semi-coupled method uses 0.01 with a total of 800 time steps for the simulation, typical for single-phase solvers. The total wall time is 435 h for the fully coupled and 5.3 h for the semi-coupled, indicating that the semi-coupled method is more computationally efficient. This is because (a) better robustness allows much larger time steps and (b) each time step is significantly faster in the semi-couple method.

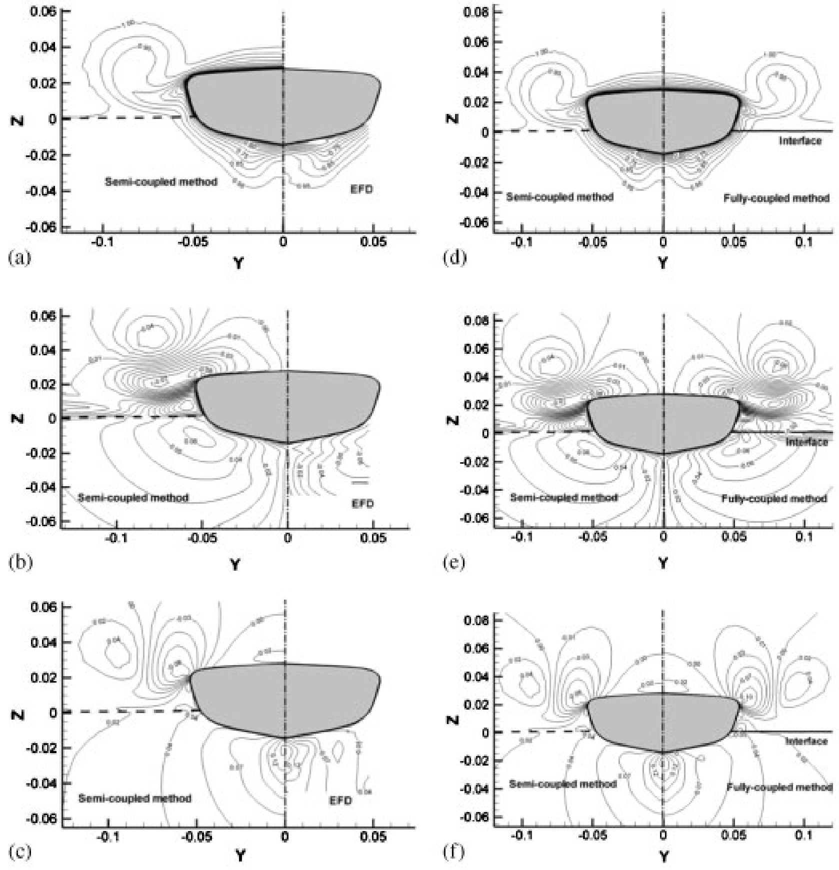

Figure 10. Comparison of velocity contour at the nominal wake plane: (a) axial velocity (u) *vs* EFD data; (b) transversal velocity (v) *vs* EFD data; (c) vertical velocity (w) *vs* EFD data; (d) axial velocity (u) *vs* fully coupled method; (e) transversal velocity (v) *vs* fully coupled method; and (f) vertical velocity (w) *vs* fully coupled method.

4.3. *Steady flow over ONR Tumblehome model DTMB 5613*

The ONR Tumblehome model DTMB 5613 with superstructure is studied in steady-state, even keel condition. The ship is advancing in a calm sea, no wind situation. Simulations are performed at high speed, corresponding to a Froude number $Fr=0.40$, and Reynolds numbers $Re_{\mathrm{w}}=6.5\times 10^6$ in water and $Re_{\mathrm{a}}=4.34\times 10^5$ in air. Air/water density and viscosity ratios are 1.2×10^{-3} and 1.8×10^{-2}, respectively. The flow in water, including large-amplitude motions, has been studied by Olivieri *et al*. [28] and Sadat Hosseini *et al*. [29], while here the flow in air is mostly analyzed.

The overset grid system includes a boundary layer, double-O topology grid with $161\times 52\times 83$ grid points, a superstructure grid with $165\times 61\times 43$ points, a skeg grid with $57\times 42\times 37$ points, a bilge keel grid with $93\times 41\times 46$, a Cartesian refinement grid for the close field with $181\times 46\times 85$, and a background Cartesian grid with $181\times 46\times 85$, for a total number of grid points of 2 807 067. The system is split into 24 blocks for parallel processing. Since the problem is symmetric with respect to the vertical centerplane, only half the ship was computed and symmetry boundary conditions used. The whole far field was set to inlet boundary condition, while no-slip was used at the ship hull. The grid spacing on the first grid point away from the wall was set such that $y^+ < 1$.

From Table II, it can be seen that the resistance coefficient in air is about 0.48% of the resistance coefficient in water, bigger than that for the 5512 case due to a much larger superstructure.

Figure 11 shows the air/water free surface and streamlines in the air region. Streamlines based on the ship coordinate system and on an earth-fixed coordinate system are shown. The streamlines are colored by axial velocity in the ship-fixed coordinate system. The orbital velocity caused by the waves is captured, as well as the separation region in the back of the ship superstructure. Three-dimensional separation structures are observed downstream of the superstructure, the flight deck, and in the transom stern. The vortical structures are more dramatic in air than in water.

Figures 12 and 13 show the vortex structure around the ship obtained by $Q = 40$ isosurfaces. Horseshoe vortices form around the ship superstructure and separate downstream. Edge vortices generate at the bow, top of the superstructure, and on the decks, all stretching along the streamwise direction after they are formed. The edge vortices from the bow and the horseshoe vortex at the superstructure interact forming a pair of counter-rotating vortices. This is clearly seen in Figure 14, which shows velocity vectors and the boundary layer at a cross-section $x = 0.55$. Separation vortices behind the ship superstructure, flight deck step, and transom show big structures. The separation vortices on the superstructure and flight deck reorient to form streamwise vortices, which interact with the deck edge vortices.

Table II. Resistance coefficient in water and air.

Water (CFD)	Air (CFD)	$\frac{\text{air}}{\text{water}}$(%) (CFD)
0.00509	0.0000244	0.48

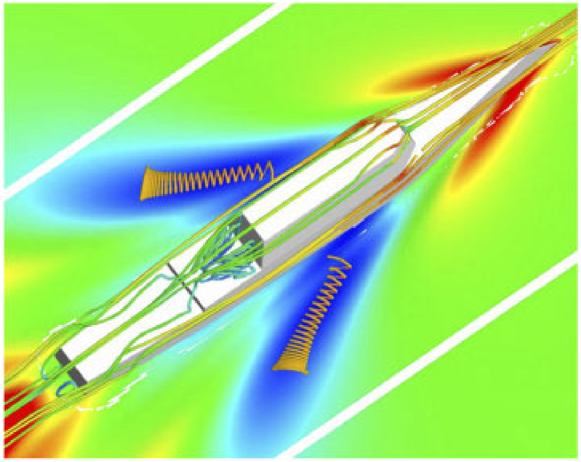

Figure 11. Free surface and streamlines for calm water and no wind.

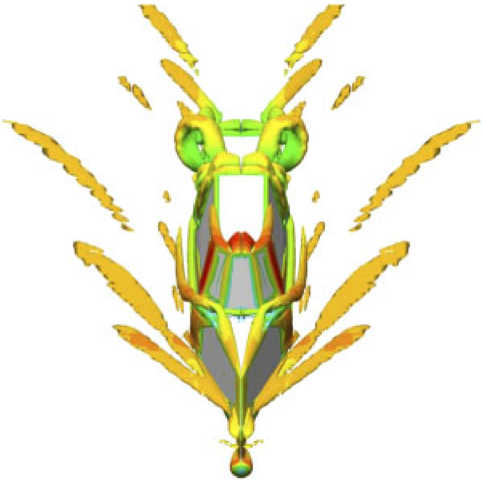

Figure 12. Front view of the vortex structure ($Q=40$ isosurfaces).

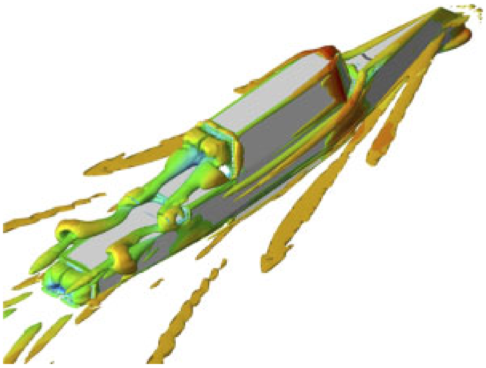

Figure 13. Side view of the vortex structures ($Q=40$ isosurfaces).

Free surface vortices are also clear in Figures 12 and 13. These vortices are stronger in air and originate from the orbital velocity present in traveling free surface waves. The orbital velocity generated by the surface waves can be clearly seen from the cross-sectional vectors of Figure 14.

The boundary layer structure in air is thicker than in water, as expected since the Reynolds number is about 15 times smaller in air than in water. The boundary layer profile is strongly affected by the many vortices present.

4.4. ONR Tumblehome in waves and wind

As shown by the resistance results for the surface combatant in Table I, the force caused by the air is small and negligible for most normal operational conditions. Large superstructures in small powering environments (as in a sailboat) or extreme winds result in non-negligible wind forces. To evaluate the effect of winds on ship motions in waves, an ONR Tumblehome in an SS7 environment

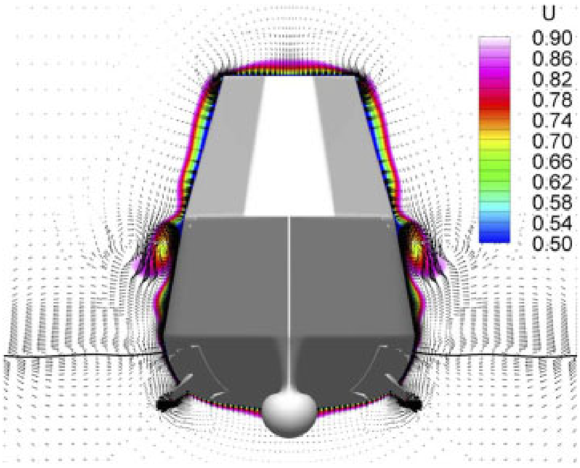

Figure 14. Velocity vectors and axial velocity for the ONR Tumblehome ship ($x = 0.55$).

is studied, with and without air forces. In an SS7, sustained winds of 70 knots cause waves with most probable wavelengths of 350 m and mean significant wave heights of 7.5 m [18]. Here a shorter wavelength (240 m) is used, still within range for an SS7. A Bretschneider frequency spectrum with a $\cos^2$ directional spectrum was used to simulate the waves, with a principal direction of incidence from the Southeast (135°). The ship has an active autopilot set to keep a North heading at a speed of 24 knots. The autopilot uses a PD speed controller with non-dimensional constants $P = 100$, $D = 100$, and a heading control with constants $P = 2$, $D = 10$. The speed controller uses the error of velocity to act on the propeller rotational speed in revolutions per minute (RPM), while the heading controller measures the error of heading between true heading and target heading and acts on the rudders to correct the course. A prescribed body force model [20] is used to simulate the twin propellers. The advance coefficient is computed based on the ship velocity, and open water curves are used to calculate the thrust forces and moments input on the equations of motion for the ship. Six degrees of freedom are used to compute the motions of the ship, as described in Carrica *et al*. [2], predicting, forward speed, sway, heave, roll, pitch, and heading.

The overset grid system is shown in Figure 15. It includes two double-O hull grids (starboard and port), a superstructure grid, skeg grid, bilge keels, twin rudders, and a Cartesian background grid, for a total of 3.85 million grid points. The background grid follows the motion of the ship in surge, sway, and yaw (horizontal motions) and is where all the far-field boundary conditions are imposed. All the ship grids (hull, skeg, bilge keels, and rudders) move following the motions predicted for the ship. In addition, the rudders rotate about the rudder axis on the ship coordinate system according to the controller directives. Thus, the rudders are children objects of the ship, in the sense that they inherit all motions from the parent object (the ship) and add their own.

Two cases were run. In the single-phase case (also termed ‘no wind’), only the water flow was solved and the forces in air ignored. The two-phase case includes the air in a semi-coupled approach, with a constant air velocity imposed in the boundary to simulate the wind. Both problems were run in an IBM P4 with 32 processors, with 120 000 grid points per processor. The computation time for a little less than 3 min of full-scale simulation (2500 time steps) was 200 wall clock hours for the two-phase computation and 150 h for the single-phase computation.

DOI: 10.1002/fld

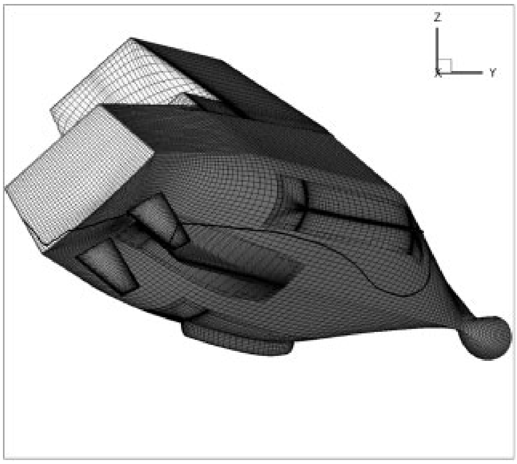

Figure 15. Overset grid system. The solid line shows the instantaneous location of the free surface on the hull.

The simulations are both started with the ship in even keel condition and zero forward speed. A transient develops where the ship accelerates to full speed while the controllers operate the rudders and propeller RPM to maintain course and speed. The results are reported in full scale to simplify the discussion but were computed at model scale. The reference velocity was set to a value of 2.84 m/s, equivalent to 34.49 knots in full scale, and corresponding to a Froude number $Fr = 0.5$. The Reynolds number in water is set to a model-scale value of $Re_{\mathrm{w}} = 9.41 \times 10^6$ and in air $Re_{\mathrm{a}} = 6.28 \times 10^5$. These Froude and Reynolds numbers are valid for the reference velocity, which is constant. The ship Reynolds and Froude numbers are constantly changing since the ship speed changes during the computation.

Two views of the free surface and air wake are shown in Figure 16. The cross-sectional contours show transversal velocity, evidencing a recirculation on the wake and the presence of an air boundary layer. At the instant shown, the ship is experiencing a broaching event in which high rolling caused by the waves, and to a less extent wind, takes one rudder out of the water greatly decreasing the steering capacity.

Figure 17 shows vector fields at two constant axial cross-sections, one at the superstructure and one at the propeller plane. The free surface is indicated with a bold line. Note the strong lateral wind blowing at the deck and the clear separation on the downstream side. Part of the starboard bilge keel is out of the water with a strong air flow on the top side. Separation also occurs on starboard near the superstructure.

As can be expected, the presence of a strong lateral wind causes the ship to lean to the downstream side (port). The average angle is, however, small. Figure 18 shows the time histories of roll, drift, and the average roll for the cases with and without wind. Note that the average rolling angle with wind is about 6°, while the case with no wind rolls is 3°. An estimation concludes that the waves are causing an average rolling angle of 3° and the wind an additional 3°. The drift angle is also slightly larger for the case with wind.

At about 90 s both simulations experience a broaching event, in which the roll angle reaches over 40° to the port side. At this point the starboard rudder loses steering control and the ship heading turns to over 25° east from the north, causing the ship starboard to face the incoming

DOI: 10.1002/fld

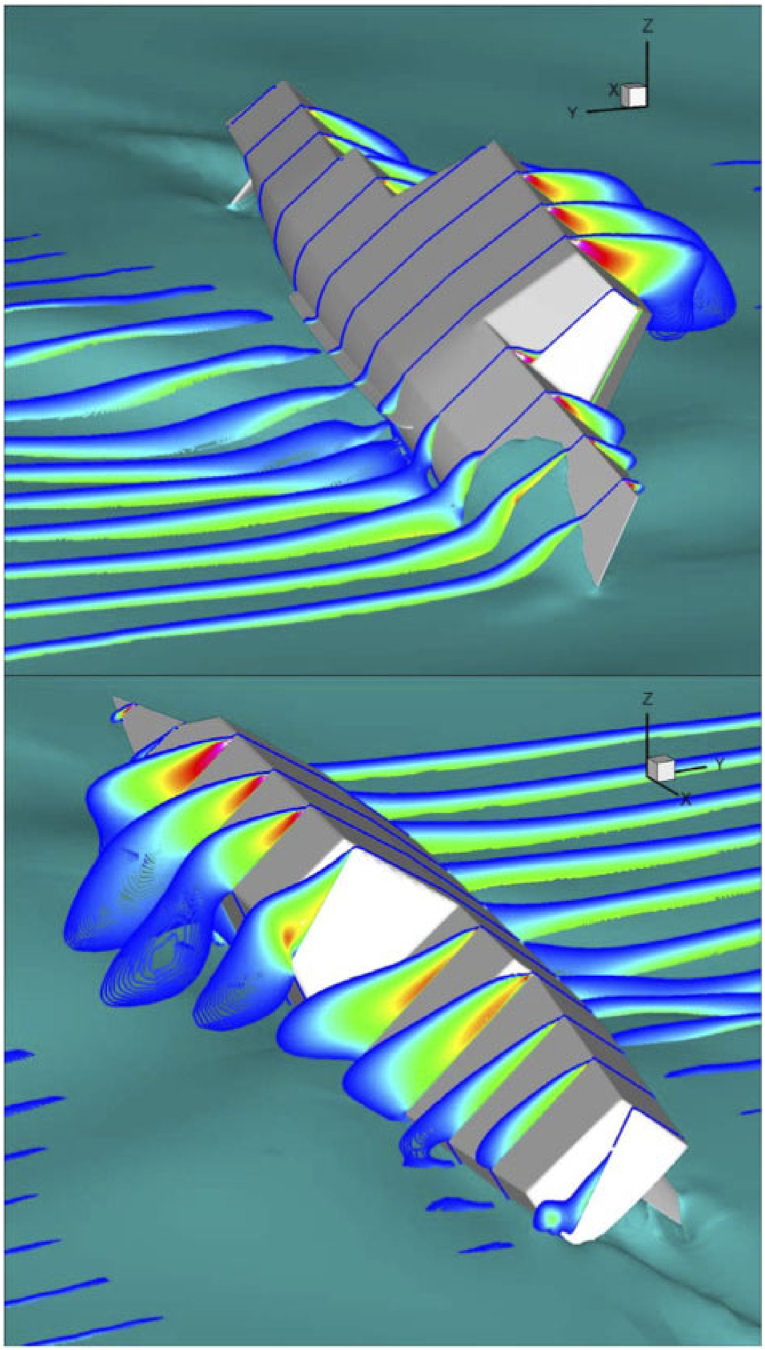

Figure 16. Two views of the free surface and cross-sectional contours of transversal velocity, showing the wake of the wind at a broaching event.

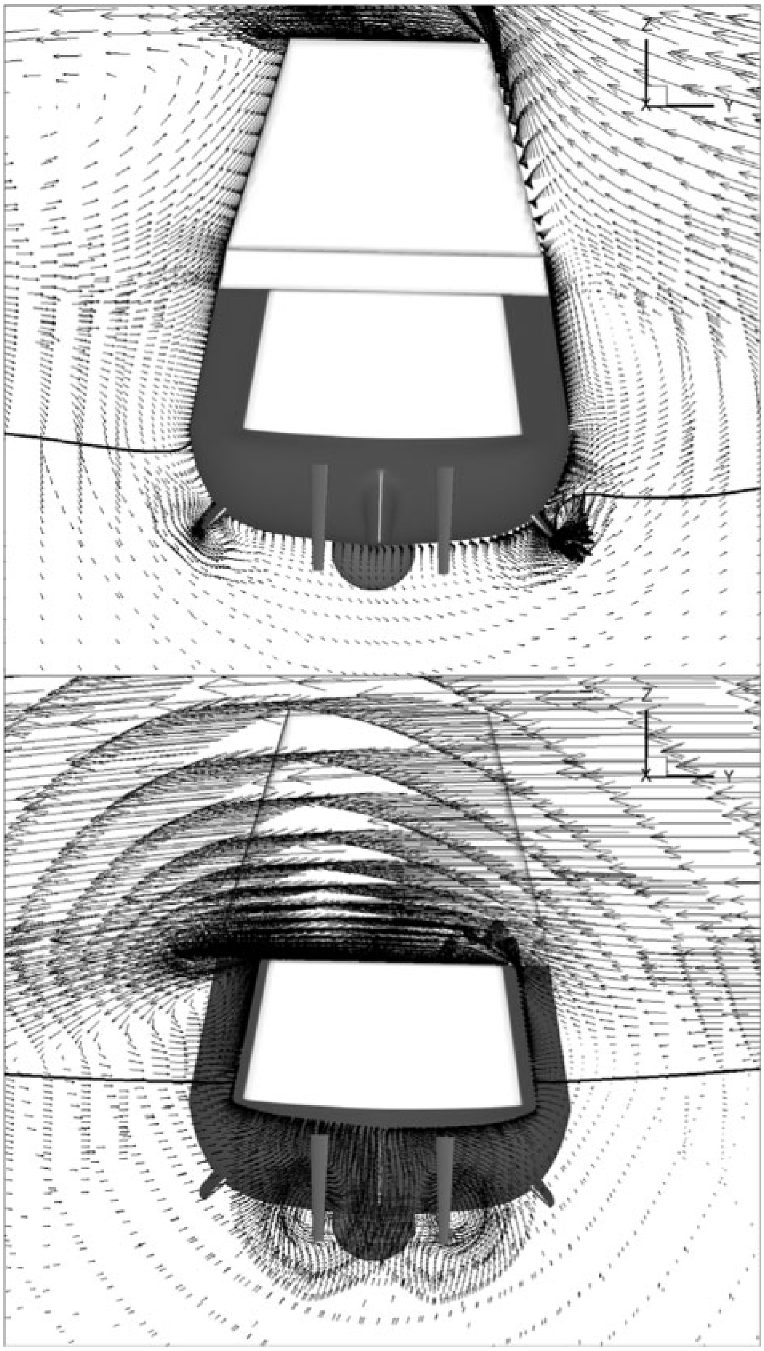

Figure 17. Velocity vectors at two cross-sections. Note the strong wind blowing over the deck, showing large separations downstream of the ship.

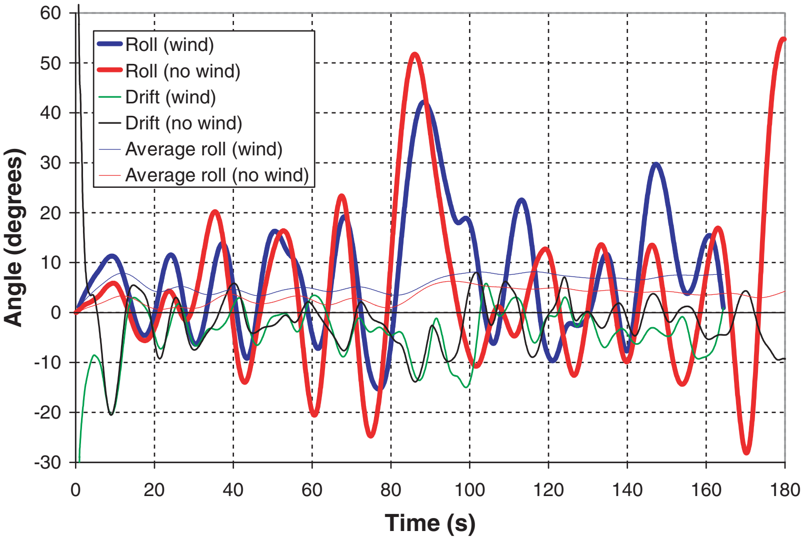

Figure 18. Time histories of roll and drift for the cases with and without wind.

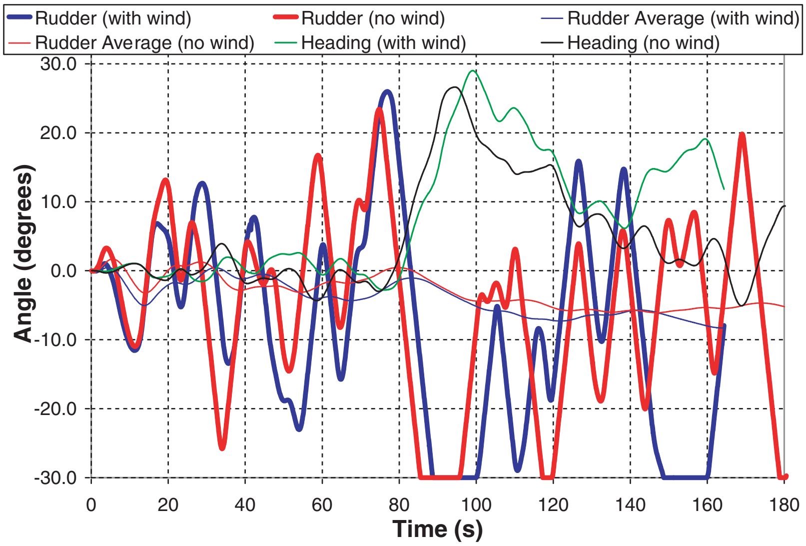

Figure 19. Rudder action and heading histories.

waves; see Figure 19. It can be seen that the case with no wind experiences a larger rolling angle than that with wind. This is possibly due to the fact that when the large wave hits the ship the case with no wind is rolling to starboard almost 10° more than the ship with wind. Note that the ship with wind rolls to starboard 15° at most, much less than the case without wind. This shows that the wind prevents rolling to starboard and limits the storage of rolling energy, thus resulting in less dramatic rolling motions. However, although the angles are smaller, large roll excursions to the port side are more frequent for the case with wind, causing less steering capability.

A second broaching event occurs at about 145 s in the case with wind and around 170 s for the case without. The case with wind also shows a smaller event (22° roll) at 110 s. In all these events the autopilot turns the rudder all the way to the port side to maintain the course. Note that after the first broaching event the case with wind takes significantly longer to recover the heading than the case with no wind and after the second broaching event loses steering capacity again.

Figure 20 shows the speed and propeller RPM histories for both cases. After accelerating to the target speed, the controller can properly maintain the ship velocity. At about 75 s the velocity drops due to a large rudder action to starboard, and the propeller RPM increases as a reaction from the controller. At the end of that process the first broaching event happens and the ship speed increases, causing a drop in the RPM. The speed control capacity is within +/−3 knots.

It is interesting to note that the powering needs are larger for the case with wind; see the higher average RPM needed in Figure 20. This behavior is anti-intuitive, since the wind has a strong component from the stern, and a thrust on the ship motion direction can be expected. While this is true, the resistance in water also increases offsetting the wind thrust. The three main causes for the bigger added resistance with wind are (a) a larger drift angle (see Figure 18) that is known to increase resistance, (b) a larger average roll angle that takes the ship to an off-design operating point (see Figure 18), and (c) the rudder action is more dramatic with wind and exhibits a larger average (see Figure 19).

The ship trajectories are depicted in Figure 21. Although the heading is well controlled up to the first broaching event, there is a noticeable drift to the west. After the first broaching event, occurring at about 950 m north, the ship loses control and turns east to the north. The case without wind recovers the north heading at about 1600 m north, but the case with wind suffers a second broaching event and keeps moving off-heading.

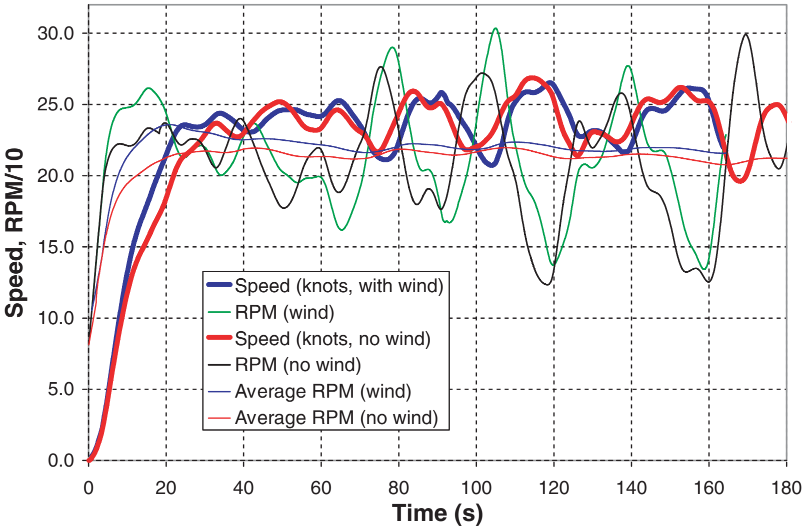

Figure 20. Ship speed and propeller RPM.

DOI: 10.1002/fld

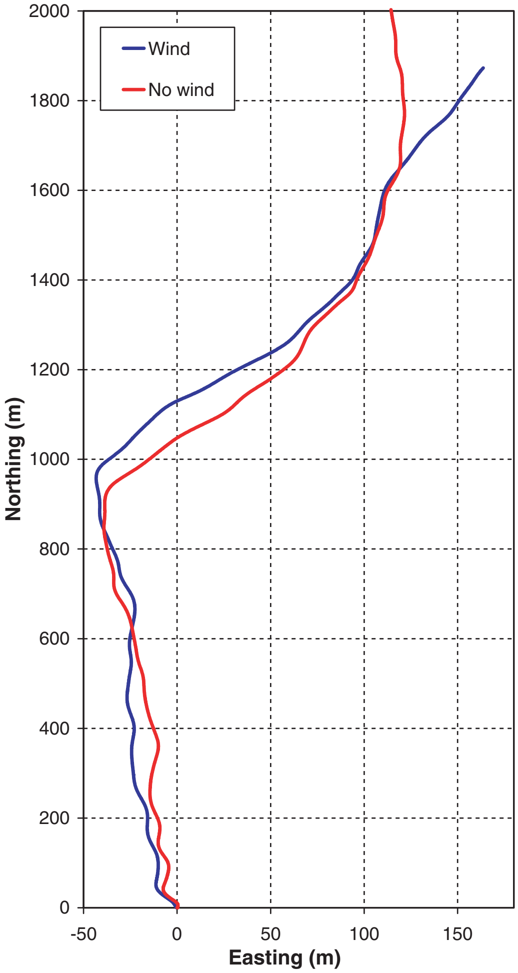

Figure 21. Ship trajectories for both cases.

5. CONCLUSIONS AND FUTURE WORK

A semi-coupled air/water level set method with dynamic overset curvilinear grids was presented. The model was designed for application to environmental effects on ship hydrodynamics. Qualitative validations were performed for laminar Couette flow over a wavy boundary, and results show good agreement with analytical solution. Validation is also done for DTMB model 5512 by comparison with the results of two-phase level set computations and EFD data, and the results show good agreement with experimental data in water and with fully coupled two-phase level set results in air and water.

The semi-coupled method is subject to the limitations of single-phase surface capturing solvers in that the air/water interface is assumed at atmospheric pressure, and thus bubbles cannot be

DOI: 10.1002/fld

resolved. An additional limitation is that the effect of the air flow on the water flow is neglected, and thus small-scale phenomena such as wave generation, spraying, etc. cannot be simulated. Two-phase fully coupled methods, such as CFDShip-Iowa version 5, can handle air/water interactions, but generally are significantly less robust and slower. The semi-coupled method can be applied to large-scale problems, such as the air flow around decks and superstructures, to analyze the effect of wind on motions and of motions on air wakes, including temperature and contaminant transport. Because of its inherent robustness, it can be used for production runs in complex geometries.

The method can be divided into two steps. At each time step the free surface flow in water is computed first with a single-phase method assuming constant pressure and zero stress on the interface. The second step is to compute the air flow assuming that the free surface is a moving IB. It is a single-phase method, thus avoiding ill-conditioned numerical systems caused by large differences in fluid properties between air and water. The IB method is extended to curvilinear grids, enforcing no-slip and divergence-free conditions for the air flow. The forcing points close to the IB can be computed and corrected under a sharp interface condition, which makes the computation very stable. Details of the overset implementation were discussed.

The air/water steady flow around the ONR Tumblehome DTMB model 5613 with superstructure has been analyzed, showing a rich set of vertical structures on the air side.

The method was further applied to analyze the motions of a DTMB 5613 in SS7 conditions with an autopilot controlling speed and course. For this problem two cases have been considered. In one of them the air flow is neglected (single-phase flow computation) and in the second the air is included with a strong 70 knot wind. Both cases experience broaching events, in which a momentary loss of steering capacity occurs. The case with wind results in a less controllable ship.

Future work includes the implementation of random gusted winds, which are often much stronger than the sustained winds and may cause capsizing and thermal and solute transport around ship. A better set of far-field boundary conditions are being developed for the air to account for the presence of boundary layers. In addition, appropriate boundary conditions for the turbulence quantities on the air side of the free surface are under study. Other refinements to the method will also be incorporated, including a better reinitialization algorithm. The implementation of transport equations to compute temperature and pollutant fields on deck is of great interest. The numerical tool will be used to guide air/water experimental model tests.

ACKNOWLEDGEMENTS

This work was supported by ONR grants N00014-01-1-0073 and N00014-06-1-0420, under the administration of Dr Patrick Purtell.

REFERENCES

1. Wilson RV, Carrica PM, Stern F. Unsteady RANS method for ship motions with application to roll for a surface combatant. *Computers and Fluids* 2006; **35**:501–524.
2. Carrica PM, Wilson RV, Stern F. Ship motions using single-phase level set with dynamic overset grids. *Computers and Fluids* 2007; **36**:1415–1433.
3. Carrica PM, Wilson RV, Noack R, Xing T, Kandasamy M, Shao J, Sakamoto N, Stern F. A dynamic overset, single-phase level set approach for viscous ship flows and large amplitude motions and maneuvering. *Proceedings of the 26th ONR Symposium on Naval Hydrodynamics*, Rome, Italy, 2006.
4. Carrica PM, Wilson RV, Stern F. An unsteady single-phase level set method for viscous free surface flows. *International Journal for Numerical Methods in Fluids* 2007; **53**(2):229–256.

DOI: 10.1002/fld

5. Reddy KR, Toffoletto R, Jones KRW. Numerical simulation of ship airwakes. *Computers and Fluids* 2000; **29**:451–465.
6. Syms GF. Numerical simulation of frigate airwakes. *International Journal of Computational Fluid Dynamics* 2004; **18**:199–207.
7. Osher S, Sethian JA. Fronts propagating with curvature-dependent speed: algorithms based on Hamilton–Jacobi formulations. *Journal of Computational Physics* 1988; **79**:12–49.
8. Hirt CW, Nichols BD. Volume of fluid (VOF) method for dynamics of free boundaries. *Journal of Computational Physics* 1981; **39**:201–225.
9. Youngs DL. Time-dependent multimaterial flow with large fluid distortion. In *Numerical Methods for Fluid Dynamics*, Morton K, Baines M (eds). Academic Press: New York, 1982; 273–285.
10. Vogt M, Larsson L. Level set method for predicting viscous free surface flows. *Seventh International Conference on Numerical Ship Hydrodynamics*, Nantes, France, 1999.
11. Cura Hochbaum A, Vogt M. Towards the simulation of seakeeping and maneuvering based on the computation of the free surface viscous ship flow. *Twenty Fourth ONR Symposium on Naval Hydrodynamics*, Fukoka, Japan, 2002.
12. Huang JT, Carrica PM, Stern F. Coupled ghost fluid/two-phase level set method for curvilinear body fitted grids. *International Journal for Numerical Methods in Fluids* 2007; **55**(8):867–897.
13. Peskin CS. Flow patterns around heart valves: a numerical method. *Journal of Computational Physics* 1972; **10**:252–271.
14. Mittal R, Iaccarino G. Immersed boundary methods. *Annual Review of Fluid Mechanics* 2005; **37**:239–261.
15. Thompson JF, Warsi ZUA, Mastin JW. *Numerical Grid Generation*. North-Holland: Amsterdam, 1985.
16. Paterson EG, Wilson RV, Stern F. General-purpose parallel unsteady RANS ship hydrodynamics code: CFDShip-Iowa. *IIHR Report 432*, Iowa Institute of Hydraulic Research, The University of Iowa, 2003.
17. Menter FR. Two-equation eddy viscosity turbulence models for engineering applications. *AIAA Journal* 1994; **32**:1598–1605.
18. Lewis E (ed.). *Principles of Naval Architecture*, vol. III. SNAME: Jersey City, NJ, 1989; 28.
19. Sullivan PP, McWilliams JC, Moeng CH. Simulation of turbulent flow over idealized water waves. *Journal of Fluid Mechanics* 2000; **404**:47–85.
20. Stern F, Kim HT, Patel VC, Chen HC. A viscous-flow approach to the computation of propeller–hull interaction. *Journal of Ship Research* 1988; **32**(4):246–262.
21. Wilson RV, Carrica PM, Stern F. Simulation of a ship breaking bow wave and induced vortices and scars. *International Journal for Numerical Methods in Fluids* 2007; **54**(4):419–451.
22. Bell JB, Colella P, Howell LH. An efficient second-order projection method for viscous incompressible flow. *Tenth AIAA Computational Fluid Dynamics Conference*, Honolulu, June 1991; 24–27.
23. Benjamin TB. Shearing flow over a wavy boundary. *Journal of Fluid Mechanics* 1959; **6**:161–205.
24. Larsson L, Stern F, Bertram V. Benchmarking of computational fluid dynamics for ship flows: the Gothenburg 2000 Workshop. *Journal of Ship Research* 2003; **47**:63–81.
25. Hino T (ed.). *Proceedings of the CFD Workshop*, Tokyo, Japan, National Maritime Research Institute, 2005.
26. Gui L, Longo J, Stern F. Towing tank PIV measurement system, data and uncertainty assessment for DTMB model 5512. *Experiments in Fluids* 2001; **31**:336–346.
27. Longo J, Stern F. Uncertainty assessment for towing tank tests with example for surface combatant DTMB model 5512. *Journal of Ship Research* 2005; **49**:55–68.
28. Olivieri A, Campana EF, Francescutto A, Stern F. Capsize high-quality data for validation of U-RANS codes. *Proceedings of the 26th ONR Symposium on Naval Hydrodynamics*, Rome, Italy, 2006.
29. Sadat Hosseini SH, Park IR, Stern F, Olivieri A, Campana EF, Francescutto A. Complementary URANS CFD and EFD for validation of extreme motions predictions. *Ninth International Conference on Numerical Ship Hydrodynamics*, Ann Arbor, Michigan, August 5–8, 2007.